

<https://doi.org/10.1038/s41529-024-00459-5>

# Corrosion resistance of additively manufactured aluminium alloys for marine applications

Check for updates

Clara Linder<sup>1,2</sup> , Bharat Mehta<sup>3,4</sup>, Salil Sainis<sup>1</sup>, Johan B. Lindén<sup>5</sup>, Caterina Zanella<sup>6,7</sup> & Lars Nyborg<sup>3</sup>

Additive manufacturing opens new possibilities for designing light-weight structures using aluminium alloys. The microstructure of two Al alloys and their corrosion resistance in NaCl and natural seawater environments were investigated. The newly designed Al-Mn-Cr-Zr based alloy showed a higher corrosion resistance than reference AlSi10Mg alloy in both environments in as printed and heat-treated conditions. The corrosion initiated in the Al matrix along the precipitates in the alloys where the Volta potential difference was found the highest. The coarser microstructure and precipitate composition of the new Al-alloy led to the formation of a resistant passive film which extended the passivity region of the Al-Mn-Cr-Zr alloy compared to the AlSi10Mg alloy. The effect of heat treatment could be seen in the microstructure as more precipitates were found in between the melt pool boundaries, which affected the corrosion initiation and slightly the pitting resistance. Overall, this study shows that a newly designed Al-alloy for additive manufacturing has a suitable corrosion resistance for applications in marine environments.

Additively Manufactured (AM) alloys represent a new frontier in materials engineering, offering unprecedented design flexibility for customized component production. This attribute empowers the creation of highly tailored alloy components, introducing a new paradigm in materials design and application. AlSi10Mg alloy was one of the first alloys to be additively manufactured by Thijs et al.<sup>1</sup> and has shown not only superior mechanical properties<sup>2</sup> but also good corrosion resistance<sup>3</sup> as compared to conventionally cast Al-Si-Mg alloy. Often, the AM material exceeds the performance of cast material counterparts<sup>4</sup>. The mechanical property improvements stem from the significantly finer microstructure because of AM powders in thin layers (typically 20–80  $\mu\text{m}$ ) being melted, remelted, and cooled rapidly. The grain size of AM material is therefore considerably smaller than cast materials and the alloying elements are evenly spread throughout the AM material compared to cast materials<sup>4,5</sup> resulting in better mechanical integrity. Furthermore, it exhibits enhanced corrosion resistance<sup>6</sup> compared to cast Al-Si-Mg alloys due to reduced volta potential differences (typically an indicator of corrosion driving force) of Si related to Al in the AM material. Owing to its attainment of very good properties and

being the first AM aluminium alloy to be synthesized, AM AlSi10Mg is often used as the benchmark alloy when investigating newer alloy compositions.

While the corrosion resistance of AM materials is higher than their cast counterparts, additively manufactured AlSi10Mg is however not immune to corrosion. This is primarily due to presence of fine Si particles in the microstructure that demonstrate a cathodic behaviour relative to Al<sup>3</sup>. For marine applications, a need exists to create even better corrosion resistant alloys. Metastable Al alloys' synthesis using non-equilibrium processing techniques have opened pathways of designing alloys with even higher corrosion resistance<sup>7</sup>, where such an improvement is observed to be due to homogeneous distribution of alloying elements and formation of super-saturated solid solution. Mn and Mg are the two most common alloying elements for solid solution strengthening of Al alloys<sup>8</sup>. Mn has a lower solubility in cast alloyed Al compared to Mg (about 2 wt. % Mn)<sup>8</sup> whereas in AM alloys, the Mn content can be increased to 5 wt. %<sup>9</sup>. Mn in general provides resistance to general corrosion both in solid solution or in the form of precipitates ( $\text{Al}_6\text{Mn}$  or  $\text{Al}_{12}\text{Mn}$ ) as it possesses solution potentials which are almost similar to the Al-solid solution matrix<sup>10,11</sup>.

<sup>1</sup>RISE, Corrosion, Vehicles and Surface Protection, Kista, Sweden. <sup>2</sup>Department of Physics, Chemistry and Biology, Linköping University, Linköping, Sweden.

<sup>3</sup>Department of Industrial & Materials Science, Chalmers University of Technology, Göteborg, Sweden. <sup>4</sup>Department of Materials Science and Engineering, KTH Royal Institute of Technology, Stockholm, Sweden. <sup>5</sup>RISE, Corrosion, Product Durability, Borås, Sweden. <sup>6</sup>Department of Materials and Manufacturing, Jönköping University, Jönköping, Sweden. <sup>7</sup>Department of Industrial Engineering, Trento University, Trento, Italy. e-mail: [clara.linder@ri.se](mailto:clara.linder@ri.se)

Other elements, such as Cr and Zr can also be added to improve the material properties of the alloy. Cr has a low solubility in Al, therefore is not a common alloying element as intermetallic phases would form and decrease the mechanical performance. There are however non-equilibrium alloying techniques which can be used to implement Cr into the Al alloy to improve the corrosion resistance. For example with ion implantation, Cr additions increased the pitting potential of an Al alloy in a NaCl environment<sup>7</sup>. The improved corrosion resistance was attributed to the presence of Cr in the protective passive film. Zr is added to Al-alloys to form Al<sub>3</sub>Zr dispersoids for increased recrystallization resistance<sup>12</sup> and higher tensile strength<sup>13,14</sup>. The addition of Zr to a 1xxx alloy improved the corrosion resistance compared to unalloyed with Zr in NaCl solution<sup>15</sup>. The higher resistance was attributed to the refinement and dispersing of other detrimental intermetallic particles such as Al<sub>3</sub>Fe when Zr is present in the alloy. However, the selected heat-treatment can impact the corrosion behaviour of Al-Mn-Si-Zn-Zr alloy as the particle distribution is affected<sup>16</sup>. Such heat treatments are beneficial for strengthening but can be detrimental to corrosion response. The primary cause is heterogeneity in the microstructures due to volta potential differences which has been studied extensively for wrought alloys while less commonly for cast alloys. However, few studies have been done on understanding the influence of microstructure on localized corrosion of AM aluminium alloys AlSi10Mg<sup>3</sup> and AA7075<sup>17</sup>.

To cover this knowledge gap, the present work attempts to investigate the influence of microstructure on the localized corrosion susceptibility. This investigation looks at novel Al-Mn-Cr-Zr based alloys which were developed previously by the authors<sup>9</sup>. The main aim of developing these alloys was to provide high temperature stability combined with general corrosion resistance (due to presence of Mn as main alloying element). The alloys were designed to gain strength with help of precipitation hardening using post AM process heat treatments. One of the Al-Mn-Cr-Zr alloys (referred to hereon as “Alloy C”) is of interest to investigate the localised corrosion behaviour, particularly its initiation and evolution as a function of second phase particles in the microstructure. The alloys AlSi10Mg (used as a benchmark), as printed Alloy C (referred to hereon as “Alloy C AP”) and heat-treated Alloy C (referred hereon as “Alloy C HT”) were exposed to immersion tests for short times of 15 min and 1 h to observe the initiation and progression of corrosion damage. Furthermore, different micro-chemical, morphological and surface potential measurements were performed, and quantitative data was statistically analysed to explain the corrosion initiation behaviour. The corrosion resistance of a newly designed AM Al-Mn-Cr-Zr based alloys was investigated in NaCl solution and natural seawater. Electrochemical and spectroscopy techniques in combination with optical, scanning electron and surface potential microscopy were used to assess corrosion behaviour of these new alloys in comparison to the AM benchmark AlSi10Mg alloy.

## Results and discussion

### Microstructural analysis

Optical microscopy results (Fig. 1) show that even though a similar bulk density (~99.8–99.9% relative density) is seen for both materials, a clear

distinction was made in the border of the samples wherein AlSi10Mg samples had lower number of pores as compared to alloy C. The reason for that is explained by printing without contours in the case of alloy C. After printing with contours, the pores were removed significantly. The images were measured using cut-section analysis in ImageJ software with a detection limit of 1 μm (assuming 6 pixels = 1 feature of 1 μm), which was considered sufficient for density estimation. The limitation of this technique is that it is a destructive method for measuring density, unlike CT scan or Archimedes method.

Electron microscopy was conducted on all three sets of samples. As shown in Fig. 2, AlSi10Mg shows a eutectic Al-Si rich solidification structure. Two different areas were studied, namely the melt pool boundaries in the bulk and border of the sample (inset 1 and 2, respectively). The difference between the two is characterised by slight difference in the interdendritic spacing between these eutectic structures suggesting a difference in cooling rates during processing<sup>18</sup>. The elemental composition as shown by EDS maps conducted at inset 1 suggests clear Si segregation at the Al-Si eutectics. The chemistry of the alloy (see Table 1) is seen to be similar to the chemistry in Table 1. Figure 3 shows the microstructure of Alloy C in as-printed condition. The alloy contains a dispersion of several nanometric precipitates, mostly Mn rich. In the centre of melt pools, more rod-/needle-shaped precipitates with sizes <100 nm in length were observed (Fig. 3 inset 2, they can also be seen in previous works<sup>19,20</sup>). At the melt pool boundaries in the bulk and the border of the sample (inset 1 and 3 in Fig. 3), slightly larger (200–400 nm) and relatively spherical in shape. These melt pool boundary precipitates in the border of the sample are relatively larger in size (~1–2 μm). EDS maps conducted at melt pool boundaries suggest enrichment of Mn, Cr at the precipitates in the bulk whereas the ones at borders are only rich in Mn. The chemistry of the alloy is seen to be slightly enriched in Mn (5.8 wt% instead of 5 wt%) as compared to base composition of the alloy (see Table 1). This suggests a slight segregation of Mn at these areas. Similar results have been reported by the authors before<sup>19</sup>. Finally, Fig. 4 shows the microstructure of peak aged alloy C. As reported before<sup>20</sup>, the microstructure is enriched in very fine Al-(Mn,Cr) containing precipitates that are formed upon direct ageing and are partly responsible for an increase in hardness of the material<sup>20</sup>. These precipitates have preferential growth at grain boundaries followed by the matrix. The melt pool boundary precipitates look slightly larger in size, but mostly similar to as-printed condition. Otherwise, similar observations to Fig. 3, with relatively larger precipitates at the border were observed.

### Particle size and Volta potential analysis

Electrochemical heterogeneities in the microstructure are the primary causes of localized corrosion in aluminium alloys. These electrochemical heterogeneities in the microstructure of different alloys were characterized by scanning kelvin probe force microscopy (SKPFM) to obtain volta potential maps as shown in Fig. 5. The Si particles in the AlSi10Mg alloy were found to be relatively cathodic to the Al matrix as these particles show higher volta potential (Fig. 5d) compared to the Al matrix they are present in. Similarly, the volta potential map of Alloy C AP and Alloy C HT (Fig. 5e and f, respectively) shows that the very fine sized Al-(Mn,Cr) precipitates

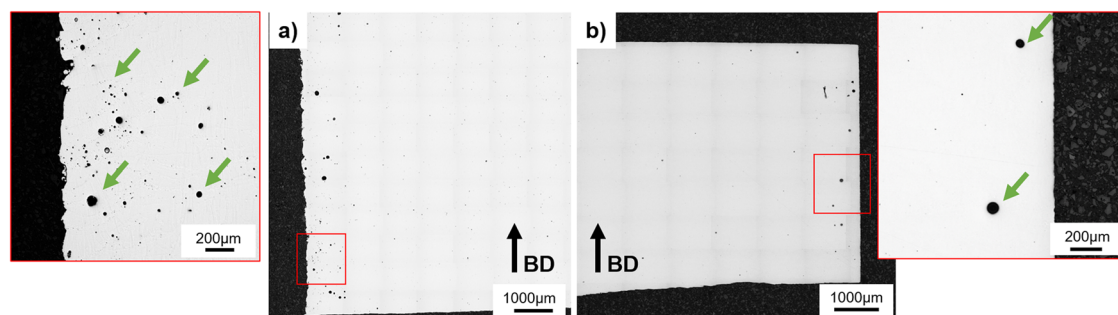
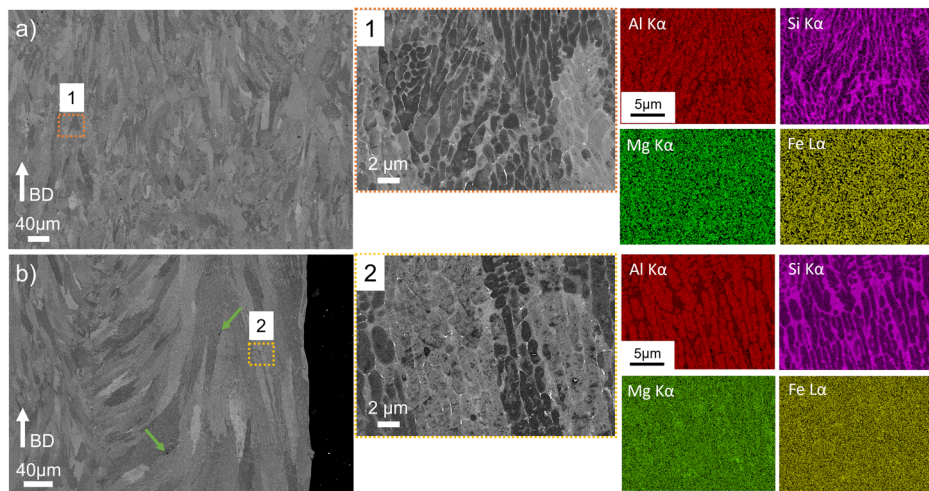


**Fig. 1 | Optical microscopy showing as-printed samples.** Images from (a) Alloy C and (b) AlSi10Mg. The insets show border porosity in both samples marked with green arrows.

**Fig. 2 | Electron microscopy for AlSi10Mg.** Images from the (a) bulk and (b) border of the sample. Inset 1 (orange) and 2 (gold) show high magnification imaging of Al-Si eutectics at melt pool boundaries at the bulk and border respectively. EDS Al, Si, Mg and Fe maps conducted on inset 1.



demonstrate cathodic characteristics as they have a relatively higher volta potential compared to the Al matrix. The volta potential difference between the particles and the Al matrix is referred hereon simply as  $\Delta V$ . The  $\Delta V$  of 40 particles in each alloy was determined from the volta potential maps and the statistics are presented in Fig. 5g. While all the particles in each three alloys are observed to be cathodic, they have a range of values whose distribution is shown though a box plot (showing the median, upper and lower quartiles and minimum and maximum values) in Fig. 5g. The spread in  $\Delta V$  values is due to the spread in particle sizes; size-volta potential relation was established by Davoodi et al.<sup>21</sup> and has also been observed in AM AlSi10Mg alloy<sup>3</sup>. Moreover, the distribution of  $\Delta V$  was also observed to be region dependant. A selection of regions from each alloy shown with white boxes on SKPFM maps and the particles'  $\Delta V$  distribution is summarized in Fig. 5g.

Susceptibility to localized corrosion is generally directly proportional to the  $\Delta V$  as has been demonstrated in various studies on different aluminium alloys<sup>3</sup>. The median  $\Delta V$  of Si particles in the melt pool boundary (MPB) at 0.23 V was higher than the median values of  $\Delta V$  of Si particles outside the MPB or in the bulk of the alloy at 0.18 V. Revilla et al.<sup>3</sup> also observed greater  $\Delta V$  values in the MPB regions ( $\sim 0.22$  V) as compared to other regions ( $\sim 0.1$  V) and the resulting localized corrosion was also greater along the MPB. In comparison, fine Si particles in a cast Al-Si have a  $\Delta V$  value 0.18 V<sup>22</sup> and coarse Si particles have a  $\Delta V$  value of 0.4 V<sup>23</sup>. In the case of Alloy C AP, two different regions containing the fine precipitates are selected: MPB containing the circular precipitates and the bulk of the alloy containing needle-like precipitates. In this alloy, the precipitates within the MPB had the lowest median  $\Delta V$ , followed by CW and greatest values in the bulk region. Comparatively, in the HT alloy C, particles within the MPB boundary  $\Delta V$  values are greater than in the bulk region.

Localized corrosion around cathodic intermetallic particles does not only depend on the volta potential, but also the geometrical characteristics such as particle size. The particle size distribution (effective diameter of a particle calculated from the measured surface area of the particles) measured using ImageJ on different microstructural regions (Fig. 6a), each with an area of  $373 \mu m^2$  is shown in Fig. 6b. Other characteristics such as cumulative number of particles, cumulative area of cathodes and length of the microgalvanic couple (MGC) interface are shown through bar plots in Fig. 6c–e,

respectively. The cumulative cathode area and the length of MGC interfaces was greatest for Si particles in AlSi10Mg alloy although the total number of cathodes is lower due to Si being a network and not discrete particles. Similar cumulative cathode areas were observed for Alloy C AP and Alloy C HT, however the number of particles in Alloy C HT was significantly higher. This indicates that the particles in the Alloy C AP are greater in size than particles in Alloy C HT as also shown in the PDF plot of Fig. 6b.

### Corrosion initiation and evolution

To understand the initiation and evolution of localized corrosion, polished samples were exposed for 15 minutes and 1 hour in 3.5% NaCl and then examined under the SEM (Fig. 7). The exposed surface is parallel to the building direction, similarly to the one examined by electron microscopy in Figs. 2–4. The corrosion attack occurs primarily in the Al matrix regions directly in the vicinity of a cathodic particles and is due to micro-galvanic coupling. In the case of AlSi10Mg, the corrosion attack morphology follows the eutectic Al-Si network, whereas for Alloy C distinct particle precipitates exist, the morphology of corrosion attack follows the shape of the particles. The likelihood of a circumferential pitting attack around particles in Alloy C depends on the  $\Delta V$  which, as shown by Davoodi et al.<sup>21</sup>, is related to the size of the cathodic particle. Since Alloy C HT contains greater fraction of small sized particles and because their  $\Delta V$  is lower, lower likelihood of pitting attack is observed on their microstructure even after 1 h immersion (Fig. 7a) compared to counterpart microstructure of Alloy C AP.

AlSi10Mg alloy showed the greatest corrosion damage as the attack is spread over an extensive area, following the morphology of the Al-Si eutectic region. While the  $\Delta V$  values for the Si particles were the lowest (Fig. 5), the greatest intensity of initial attack is attributed to the much greater geometrical characteristics (Fig. 6). Since the total and cumulative cathodic area length is the greatest, there is much higher susceptibility to corrosion attack. The other two alloys Alloy C AP and Alloy C HT showed similar initial localized corrosion values. Alloy C AP and HT have porosities and tentatively coarser precipitates in melt pool boundaries and the outer layers (Fig. 1) and that is where the corrosion initiated. This indicates that the porosities or coarser precipitates are possible corrosion initiators<sup>24</sup>. AlSi10Mg was printed with a contour which reduced the porosities in the border of the alloy considerably and the corrosion attacks were not as localised as in Alloy C. Thus, the presence or not of a contour in the printing strategy seems to primarily affect the initiation of corrosion.

It is however noteworthy that in Alloy C AP, the initial attack preferentially occurs over the rod-/needle- shaped precipitates, owing to them having much greater  $\Delta V$  values than the other precipitates. An inset in Alloy C AP after 15 min exposure shows the higher magnification image of attack around such particles. It is observed that the intensity of attacks is greater around them as compared to fine round precipitates. In the case of Alloy C

**Table 1 | Summary of composition from EDS chemical analysis in the bulk of the sample for the alloys studied**

Alloy	Al	Mn	Cr	Zr	Fe	Si	Mg
AlSi10Mg	Rem.	–	–	–	0.3	10.7	0.3
Alloy C AP	Rem.	5.8	0.8	0.8	0.3	0.1	–
Alloy C HT	Rem.	6	0.7	0.6	0.3	0.2	–



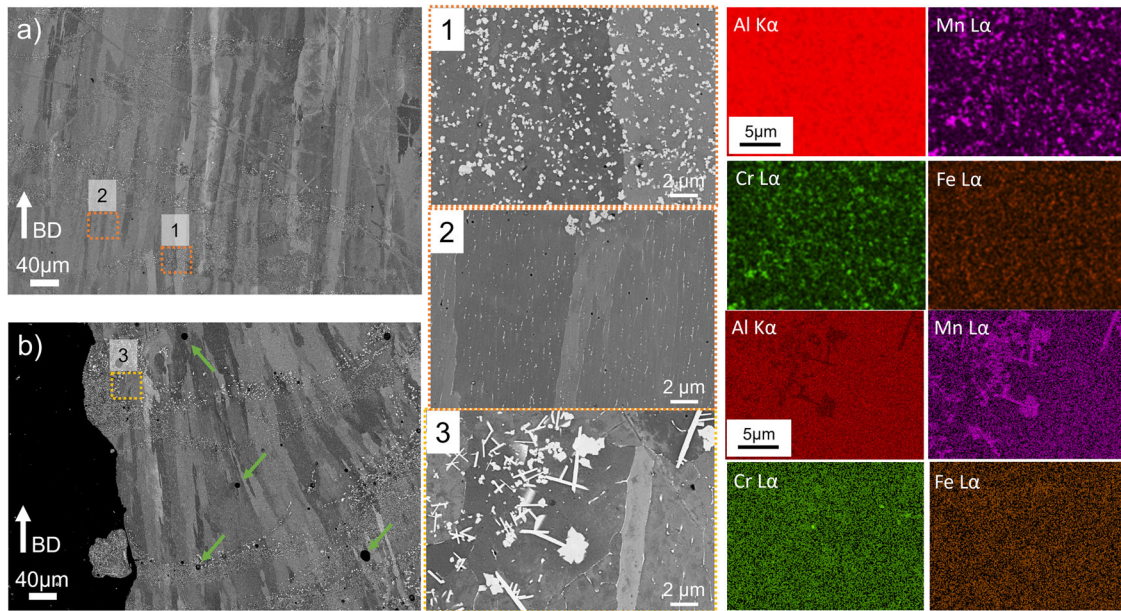


**Fig. 3 | Electron microscopy for Alloy C as-printed condition.** Images from the (a) bulk and (b) border of the sample. Inset 1 (orange) and 2 (orange) show high magnification image of microstructure at melt pool boundaries and centre of melt pool at bulk. Inset 3 (gold) shows high magnification imaging of microstructure at melt pool boundaries at border of the sample. EDS Al, Mn, Cr and Fe maps conducted on inset 1, 2. Sub-surface pores in border of the sample are marked in green.

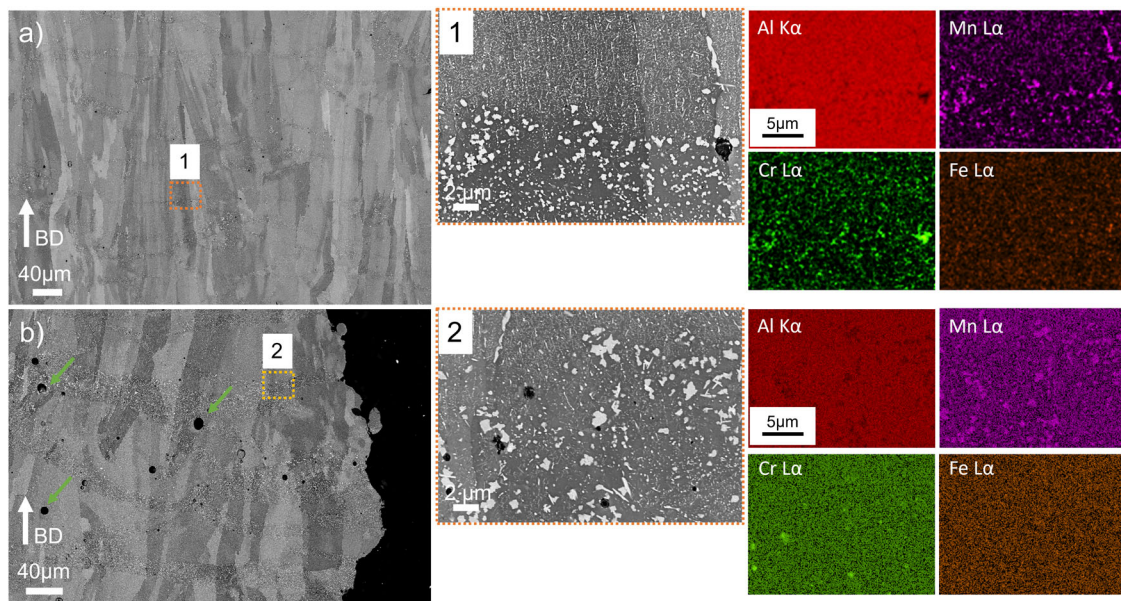


**Fig. 4 | Electron microscopy for Alloy C peak aged condition.** Images from the (a) bulk and (b) border of the sample. Inset 1 (orange) and 2 (gold) show high magnification imaging of microstructure at melt pool boundaries at bulk and border respectively. EDS Al, Mn, Cr and Fe maps conducted on inset 1, 2. Sub-surface pores in border of the sample are marked in green.

HT, the particles in the MPB show greatest susceptibility to localized corrosion attack and is due to them having a greater  $\Delta V$ .

Prolonged exposure to 3.5% NaCl for 24 h was performed to evaluate similarly the extent of corrosion damage and the results are presented in Fig. 8. The SEM microstructures in Fig. 8a show the morphology of corrosion attacks. It can be seen that the localized corrosion that started due to microgalvanic coupling between Al-Si in the AlSi10Mg alloy has progressed into more severe form as the corrosion products are observed to be formed over most of the surface of the alloy. Comparatively, the micrographs of the corroded surfaces of Alloy C AP and Alloy C HT do not show widespread corrosion product spread but the localized damage is more intense than that

seen for shorter exposures (Fig. 7). The cumulative area of corrosion attack was found greater for Alloy C AP compared to Alloy C HT.

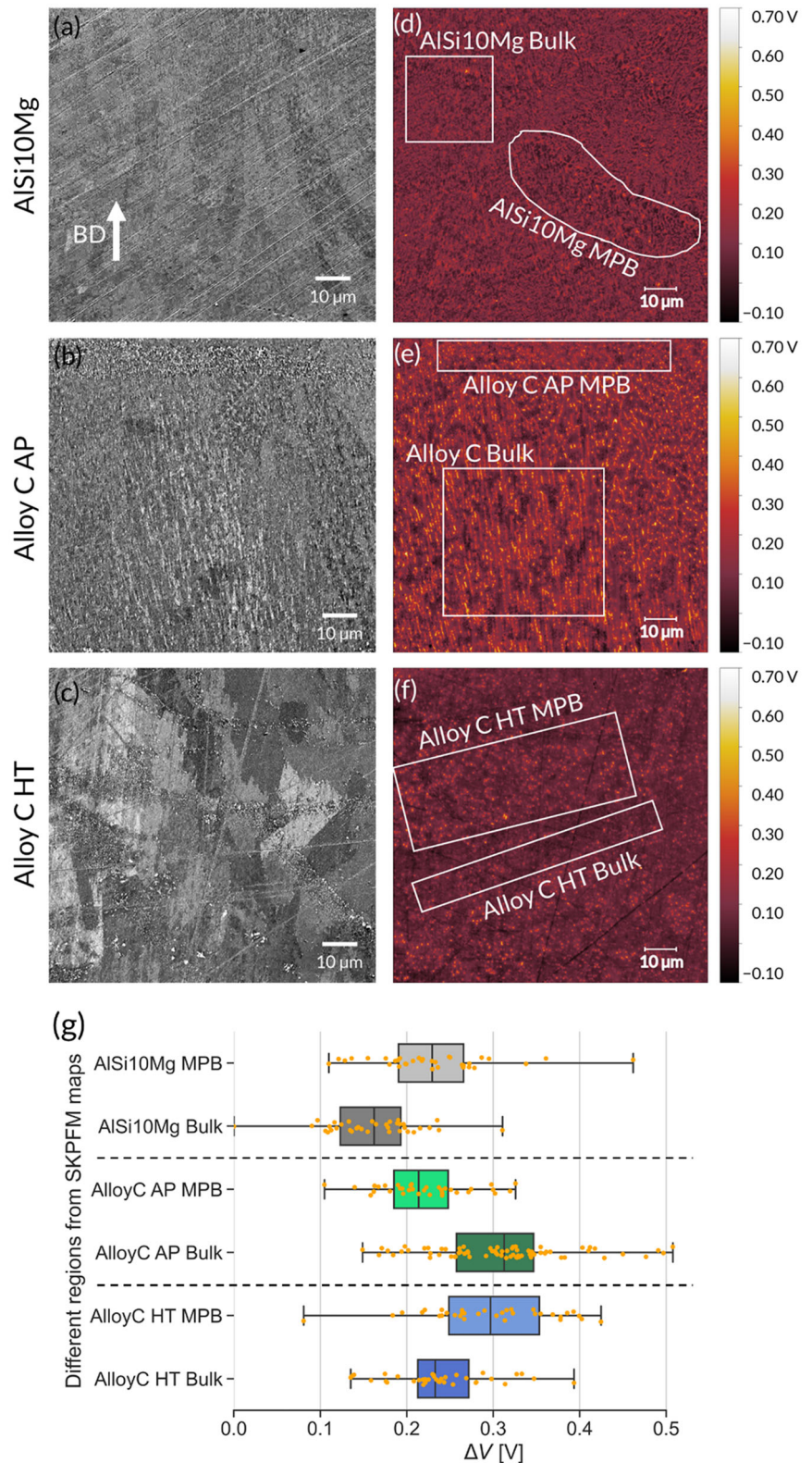
So, while during the corrosion initiation, the  $\Delta V$  provides the driving force for localized corrosion, it is the particle density in the local region of the microstructure that dictates how intense the corrosion attack is at longer exposures.

#### Electrochemical investigation of corrosion resistance in NaCl and natural seawater

Potentiodynamic polarisation (PD) measurements were carried out after 1 day of exposure to 3.5% NaCl and natural seawater (Fig. 9).



**Fig. 5 | Volta potential analysis.** SEM micro-structure of different regions in (a) AlSi10Mg (b) Alloy C – AP (c) Alloy C – HT, (d–f) SKPFM maps showing volta potential of the corresponding regions (g) box and scatter plot showing the  $\Delta V$  of particles within the different white boxes indicated in SKPFM maps.



In the PD curves, at potentials more positive than the corrosion potential  $E_{corr}$ , all materials (except AlSi10Mg in seawater) have a passive region until the critical pitting potential ( $E_{pit}$ ) is reached. AlSi10Mg in seawater does not have a passive behaviour and is constantly active. Its corrosion potential however is the highest of all materials. The passive

region for AlSi10Mg is much shorter compared to Alloy C. This means the passive film formed on the surface of Alloy C is more stable and less active than AlSi10Mg. The passive film of Alloy C is also more resistant to pitting corrosion compared to AlSi10Mg, which can be seen from the higher pitting potential.

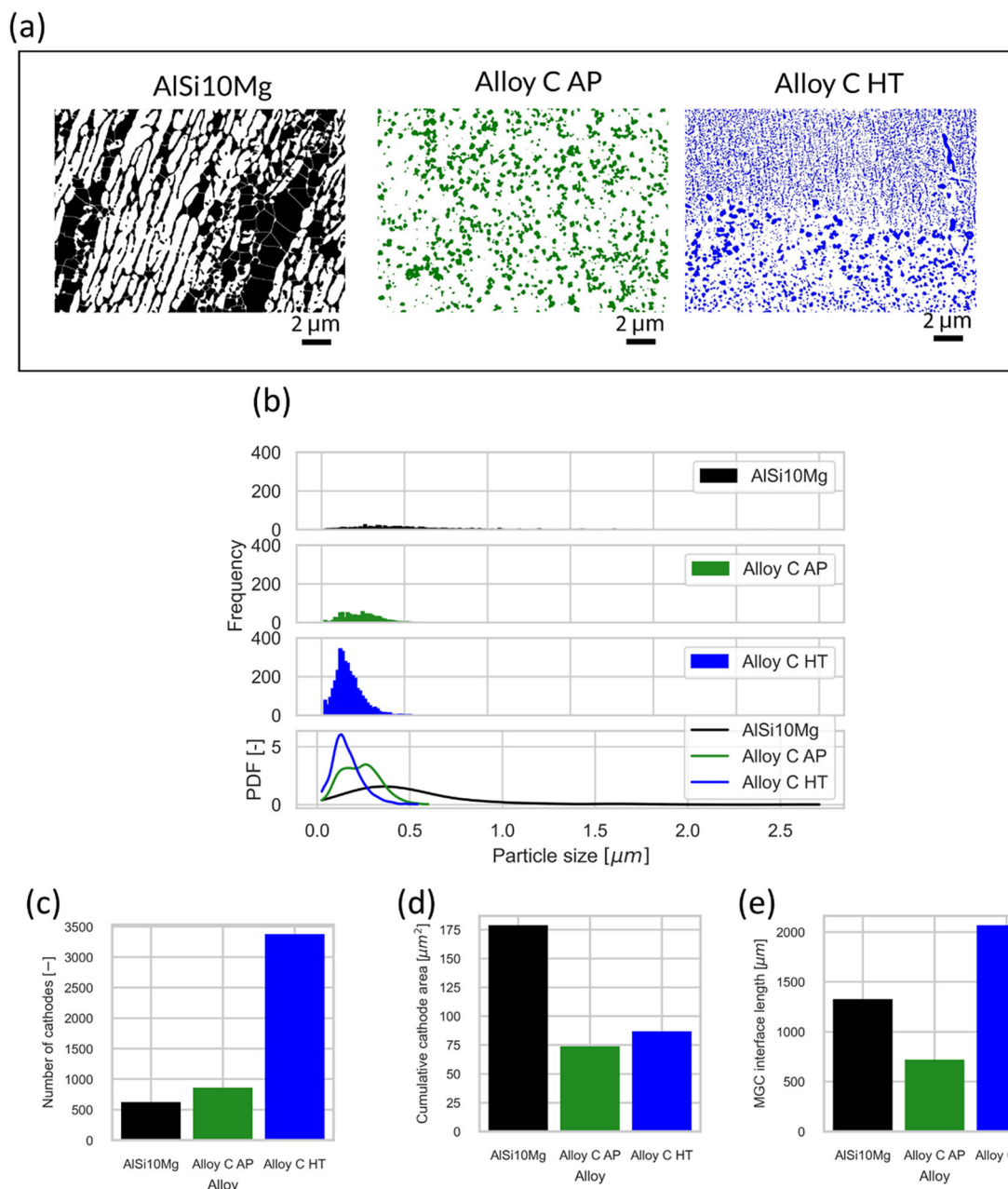


**Fig. 6 | Particle geometrical characteristics obtained using ImageJ on SEM micrographs (373 μm<sup>2</sup>).** (a) Cathodic particles in the three alloys (b) particle size distribution and probability density function (PDF) (c) Number of cathodic particles (d) cumulative area of cathodic particles (e) cumulative length of MGC interfaces.

The corrosion potential  $E_{\text{corr}}$ , corrosion current density  $i_{\text{corr}}$ , passive current density  $i_{\text{pass}}$  and pitting potential  $E_{\text{pit}}$  were extracted through Tafel extrapolation and presented in Table 2.

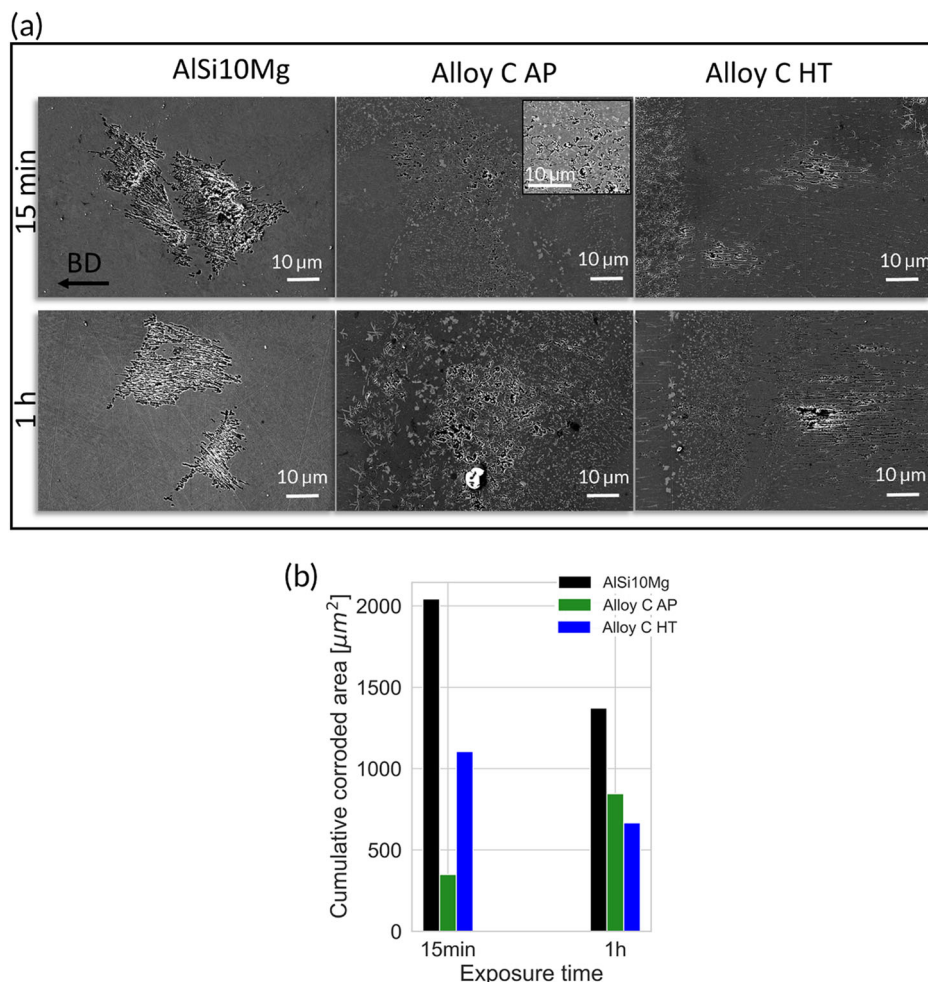
Alloy C samples (AP and HT) have significantly lower corrosion and passive current densities compared to AISi10Mg in both NaCl and seawater, thus the corrosion resistance of Alloy C is considerably higher than AISi10Mg. However, the corrosion current density is higher in seawater compared to NaCl. This can be explained by the difference in electrolyte composition, i.e. natural seawater contains anions other than Cl<sup>-</sup> such as SO<sup>4-</sup>, HCO<sup>3-</sup> and Br<sup>-</sup>. These anions are expected to play a larger role in the breakdown of the passive layers<sup>25-27</sup>. The pitting potential of heat-treated samples is slightly more negative (-0.1 V) in NaCl compared to the as-printed condition, which could indicate the heat-treatment seem to slightly decrease the corrosion resistance of Alloy C. This could be caused by the presence of the grain-boundary precipitates that affects localized corrosion.

Electrochemical Impedance Spectroscopy (EIS) were carried out after 1 day of exposure to 3.5% NaCl and natural seawater. The Bode and Nyquist plots of the recorded data is shown in Fig. 10.

The data was then fitted with an equivalent electronic circuit based on the Randles circuit with a constant phase element. The results from the fit are shown in Table 3.

In NaCl the total impedance at low frequency is very different for AISi10Mg compared to Alloy C, i.e. 3.7 kΩ vs 272 kΩ for Alloy C AP and 446 kΩ for Alloy C HT. The two order of magnitude difference could also be seen in the corrosion current densities, confirming once again that the surface of AISi10Mg is considerably more active than Alloy C in NaCl. In natural seawater the difference between the alloys is also seen but not as pronounced, i.e., 13 kΩ for AISi10Mg, 56 kΩ for Alloy C AP and 44 kΩ for Alloy C HT, in agreement with the corrosion current densities. In the Nyquist plots, the larger semi-circles for Alloy C in both environments

**Fig. 7 | Corrosion initiation in NaCl.** **(a)** SEM images of exposed samples AlSi10Mg, Alloy C AP and Alloy C HT after different immersion times of 15 min and 1 h in 3.5% NaCl and **(b)** quantitative analysis of the cumulative corroded area in each of the alloys' microstructures.



compared to AlSi10Mg is in line with the Bode total impedance trends, i.e. that Alloy C has a higher corrosion resistance. The two orders of magnitude difference in charge transfer resistance ( $R_{ct}$ ) from the fitted data for NaCl samples is also in agreement with the corrosion current densities in Table 2 and the total impedances. In natural seawater, the charge transfer resistance of Alloy C is higher than AlSi10Mg, but not as predominantly as in NaCl. The capacitance values are lowest for Alloy C in both environments, which indicates a denser passive film compared to AlSi10Mg. For the phase angle values, in NaCl AlSi10Mg seems to present one time constant, whereas Alloy C presents a broader peak which could be an overlap of two time constants as it has been seen for AlSi10Mg. This would indicate a slow diffusion process at lower frequencies was detected for Alloy C and not for AlSi10Mg<sup>28</sup>. In seawater all three alloys present the broader peak as seen for Alloy C in NaCl, which would indicate that the behaviour of AlSi10Mg is different in seawater compared to NaCl. This difference in behaviour was not seen for Alloy C. The maximum phase angle for Alloy C is shifted towards higher frequencies compared to AlSi10Mg which indicates higher passive film barrier properties and higher resistance<sup>29</sup>. Overall, the impedance data is in agreement with the potentiodynamic polarisation curve data that the corrosion resistance of Alloy C is higher than AlSi10Mg in both NaCl and seawater. The overall higher corrosion resistance of Alloy C is attributed to the formation of a protective passive film with high resistance at OCP (Fig. 10) and also at higher potential as the critical pitting potential is high (Fig. 9 and Table 2). The coarser microstructure with larger precipitates of Alloy C seems to favour the formation of the passive layer compared to the finer eutectic structure of AlSi10Mg.

Passivity is broken down over heterogeneous phases and since AlSi10Mg has the greatest area fraction of cathodic Si phase as compared to

area fraction of cathodic phases in both as printed and heat-treated Alloy C (Fig. 6c) the AlSi10Mg also has the least corrosion resistance. Lowest passivity is also reflected in the extensive corrosion initiation damage (Fig. 7a) even at very short immersion times. The corrosion damage to the Al in the Al-Si eutectic extended over a large area as compared to much more localized corrosion damage initiation around fine and coarse precipitates in Alloy C (Fig. 7a). This is reflected also in the quantitative analysis shown in Fig. 7b where the total initial corroded area was also very high for AlSi10Mg alloy compared to as printed and heat-treated Alloy C. The passivity of AlSi10Mg surface was poor after 24 h exposure, majority of the surface was covered with corrosion products. Relatively, alloy C showed higher corrosion resistance because the corrosion was localized over and around precipitates. Heat treated Alloy C shows better corrosion resistance than as printed Alloy C due to dispersion of Zr and Cr containing precipitates into much finer features, which has been observed and reported in studies of Jia et al.<sup>12</sup> and Kim et al.<sup>15</sup>.

In summary, two Al alloys have been additively manufactured by laser powder bed fusion, their microstructure analysed and their corrosion resistance in NaCl and natural seawater have been evaluated. The microstructure of the AlSi10Mg presents a fine eutectic Si network, whereas Alloy C has Mn enriched nano precipitates mainly concentrated in the melt pool boundaries. After heat treatment precipitates in between the melt pools had grown slightly combined with a global formation of fine Mn rich precipitates in the matrix. In AlSi10Mg the corrosion initiated in the eutectic Al-Si regions, in Alloy C more localized attack around the particles in the melt pool boundaries were observed.

The corrosion resistance in NaCl and natural seawater environments was investigated. Alloy C showed a higher corrosion resistance than



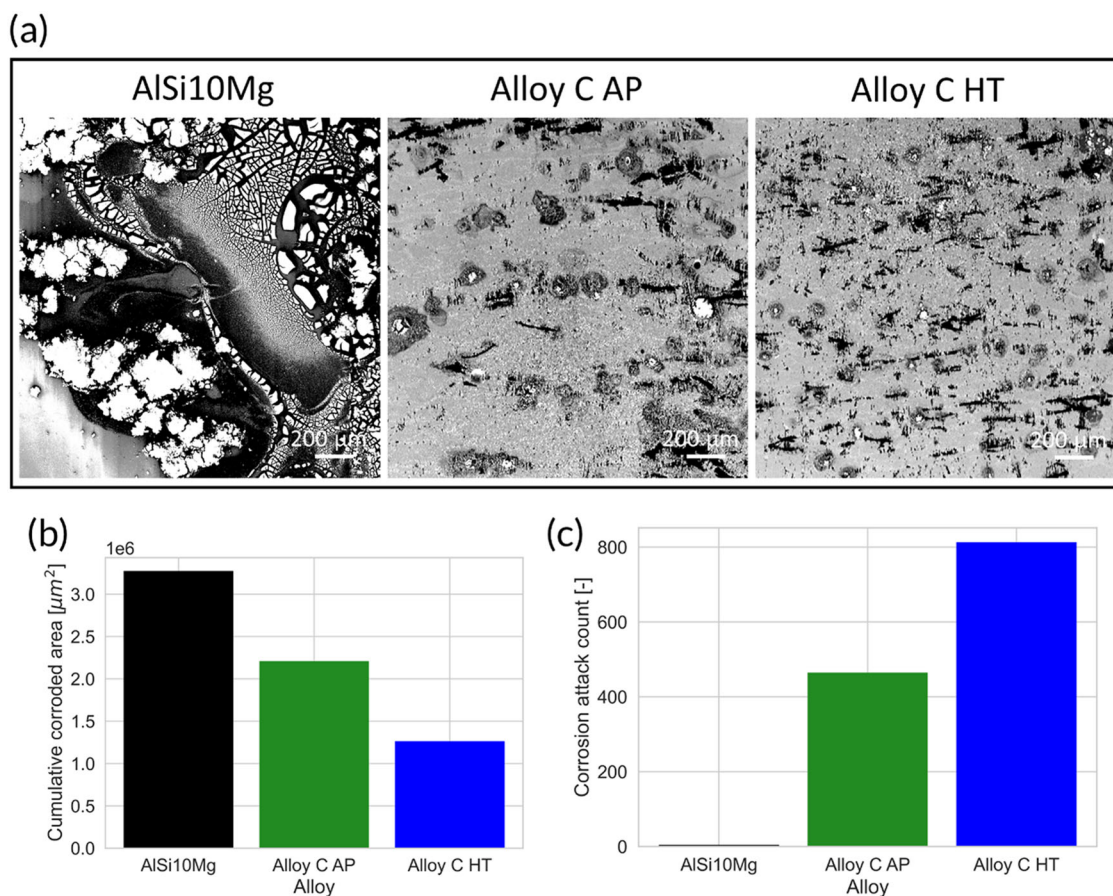


**Fig. 8 | Corrosion evolution after 24 hours of exposure.** **a** SEM micrographs of corroded samples of the three different alloys after 24 h immersion exposure, **b** cumulative corroded area measured using ImageJ analysis of micrographs in (a); **c** Cumulative number of corrosion attacks.

reference AlSi10Mg in both environments in as-printed and heat treated condition. The corrosion current densities and total impedance values were one to two orders of magnitude higher for Alloy C compared to AlSi10Mg. The corrosion initiated in the Al matrix along the precipitates in the alloys where the Volta potential difference was found the highest. The cumulative cathode area in AlSi10Mg was almost double compared to Alloy C which explains to higher susceptibility to corrosion of AlSi10Mg compared to the newly designed Al-Mn-Cr-Zr alloy.

## Methods

### Raw material

Pre-alloyed Al-Mn-Cr-Zr powder manufactured using nitrogen gas atomization process was provided by Höganäs AB, Sweden. Standard AlSi10Mg powder was sourced from EOS GmbH, Germany. The alloy chemistry and powder size distribution are provided in Table 4.

### Manufacturing methods and post processing heat treatments

All the materials were processed using powder bed fusion-laser beam (PBF-LB) process in an EOS M290 machine with a Yb-fiber laser of 400 W (370 W nominal) power. [8] Laser power (370 W), laser speed (1300 mm/s), hatch distance (0.13 mm), scan rotation ( $67^\circ$  between each layer), and layer thickness (0.03 mm) were employed to produce fully dense samples (> 99.7% relative density). Some of the samples were heat treated based on previous knowledge of optimised heat treatments or heat treatments suggested by machine manufacturer<sup>20,30</sup>. The heat treatments were conducted in a pre-heated resistance furnace with a secondary thermocouple to verify the temperature close to the sample and keep a temperature control of  $\pm 2^\circ\text{C}$ . Samples were printed in  $105 \times 10 \times 12$  mm. Table 5 Summarizes the printing parameters used and heat treatments applied on the samples.

### Structural and chemical characterisation

For microstructure analysis, samples were cut close to the centre of XZ plane (along building direction) a few mm from the edge followed by mounting the samples in an epoxy-based conductive thermoset resin. The samples were coarse grinded and polished up to 1  $\mu\text{m}$  grit size followed by a final OP-S silica-based polish for electron microscopy. The samples were prepared using a Struers Tegra Pol 31 machine. Light optical microscopy was conducted using a ZEISS AxioScope 7 machine with an automated scale enabling the stitching of larger cross sections ( $10\text{--}20$  mm<sup>2</sup>) at 10X optical zoom for each image, providing 0.4  $\mu\text{m}$ /pixel accuracy. Electron microscopy was done using a Zeiss Gemini 450 SEM equipped with a field emission gun source containing a size channel back scatter detector. The SEM is fitted with an Oxford Instruments ULTIM MAX Energy Dispersive X-ray Spectroscopy (EDS) detector, which enabled elemental mapping of microstructure at sub-micron resolutions. Acceleration voltage of 5 kV with probe current of 1 nA was used.

Electrochemical heterogeneity in the microstructures of the three different alloys was characterized using a Park Systems NX10 Scanning Kelvin Probe Force Microscope (SKPFM) in the Electric Force Microscopy (EFM) mode. An ElectriMulti75-G EFM probe was used that had a tip diameter <25 nm and a resonant frequency of 75 kHz. The set point of the measurement was 2 nm and the tip was biased at 5 V for the measurement.

Samples for exposure to NaCl followed by SEM analysis were prepared in the same manner as above. The analysis was carried out with a Zeiss Gemini 300 SEM equipped with an Oxford X-Max<sup>N</sup> EDS detector. Acceleration voltage was 10 kV.

Microstructure and corrosion damage quantification was performed with ImageJ. Due to the microstructure being complex, two plugins were adopted. Firstly, Trainable Weka Segmentation plugin was



**Fig. 9 | Potentiodynamic polarisation curves recorded after 1 day of exposure. (a) 3.5% NaCl at room temperature and (b) natural seawater, scan rate 1 mV/s.**

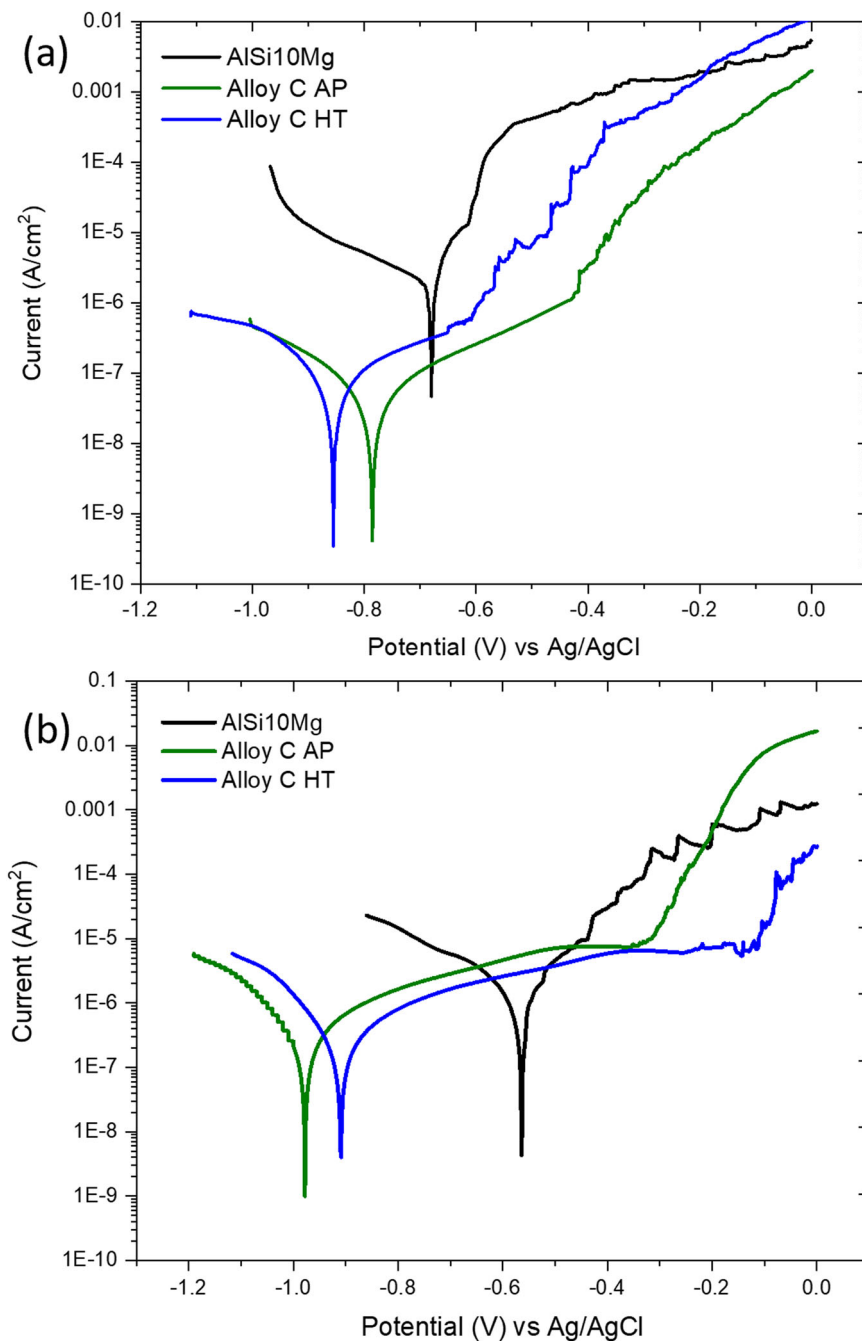


**Table 2 | Corrosion potential ( $E_{corr}$ ), corrosion current density ( $i_{corr}$ ), passive current density ( $i_{pass}$ ) and pitting potential ( $E_{pit}$ ) extracted from polarisation curves in Fig. 9**

	Environment	$E_{corr}$ (V)	$i_{corr}$ ( $\mu\text{A}\cdot\text{cm}^{-2}$ )	$i_{pass}$ ( $\mu\text{A}\cdot\text{cm}^{-2}$ )	$E_{pit}$ (V)
AlSi10Mg	NaCl	$-0.73 \pm 0.01$	$2.95 \pm 0.54$	$22.04 \pm 9.17$	$-0.61 \pm 0.00$
	Seawater	$-0.60 \pm 0.03$	$2.07 \pm 0.29$	–	–
Alloy C-AP	NaCl	$-0.71 \pm 0.09$	$0.036 \pm 0.01$	$1.60 \pm 0.39$	$-0.36 \pm 0.10$
	Seawater	$-0.98 \pm 0.01$	$0.31 \pm 0.03$	$7.53 \pm 0.08$	$-0.38 \pm 0.02$
Alloy C-HT	NaCl	$-0.82 \pm 0.05$	$0.035 \pm 0.02$	$1.39 \pm 0.14$	$-0.48 \pm 0.06$
	Seawater	$-0.91 \pm 0.01$	$0.34 \pm 0.09$	$4.25 \pm 2.1$	$-0.32 \pm 0.15$

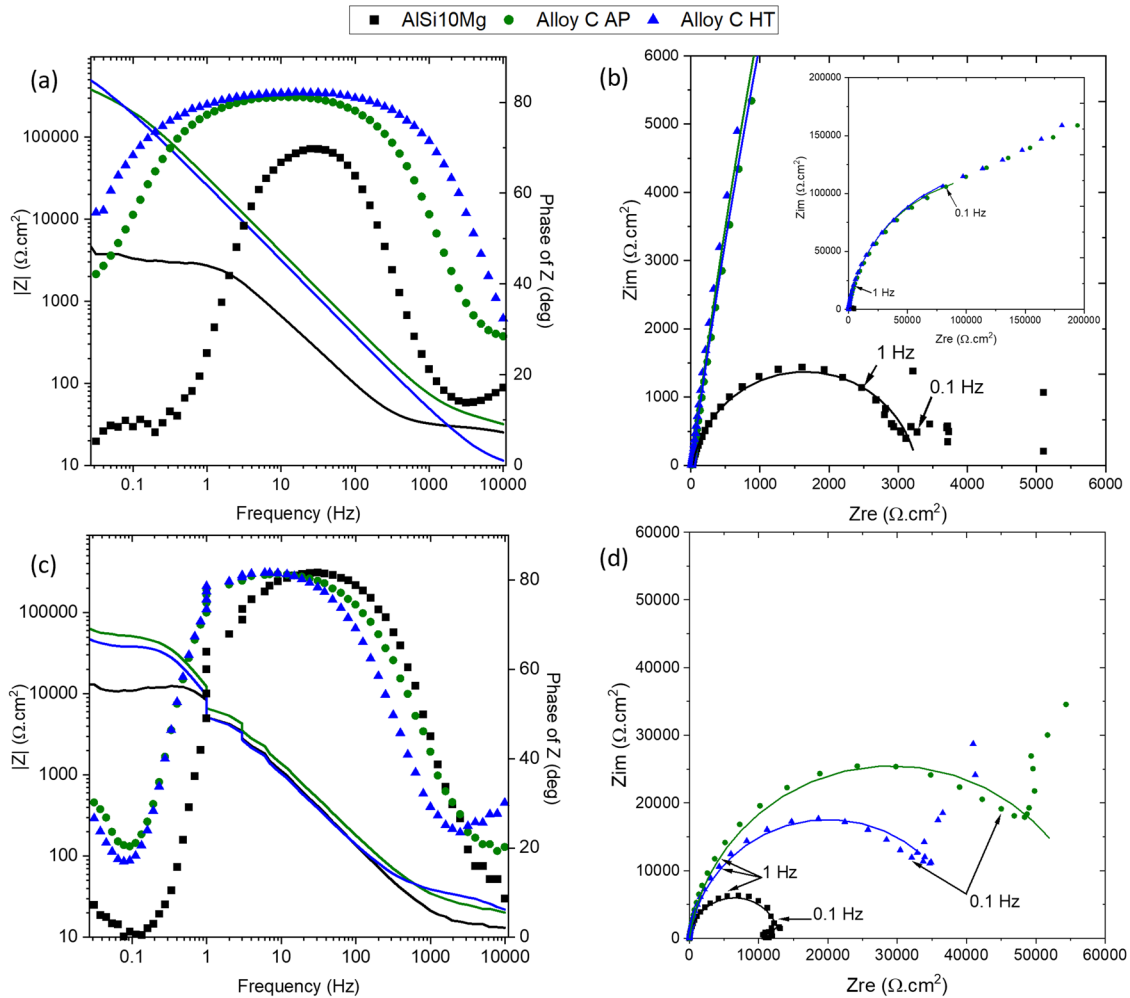


**Fig. 10 | Bode plots and Nyquist plots of EIS data. (a, b)** 3.5% NaCl, zoom-in on high frequency data and full data in insert of the Nyquist plot and **(c, d)** natural seawater after 24 hours exposure.

**Table 3 | EIS parameters extracted from the fitting of the Nyquist plots at high frequencies**

		$R_s$ ( $\Omega \cdot \text{cm}^2$ )	$Y_0$ ( $\Omega^{-1} \cdot \text{cm}^{-2}$ )	$n$	$R_{ct}$ ( $\Omega \cdot \text{cm}^2$ )	Chi-square
AlSi10Mg	NaCl	$22.0 \pm 5.1$	$3.4 \times 10^{-5} \pm 1.8 \times 10^{-6}$	$0.89 \pm 0.01$	$3.2 \times 10^3 \pm 1.9 \times 10^2$	$5.7 \times 10^{-3}$
	Seawater	$19.8 \pm 5.7$	$1.6 \times 10^{-5} \pm 1.6 \times 10^{-7}$	$0.94 \pm 0.01$	$1.1 \times 10^4 \pm 1.3 \times 10^3$	$3.6 \times 10^{-3}$
Alloy C – AP	NaCl	$17.5 \pm 6.0$	$6.8 \times 10^{-6} \pm 6.9 \times 10^{-8}$	$0.91 \pm 0.01$	$2.5 \times 10^5 \pm 2.6 \times 10^4$	$1.8 \times 10^{-4}$
	Seawater	$20.6 \pm 1.6$	$1.7 \times 10^{-5} \pm 1.6 \times 10^{-6}$	$0.92 \pm 0.01$	$7.5 \times 10^4 \pm 1.3 \times 10^4$	$6.8 \times 10^{-3}$
Alloy C-HT	NaCl	$10.8 \pm 0.3$	$7.6 \times 10^{-6} \pm 3.9 \times 10^{-7}$	$0.92 \pm 0.01$	$1.3 \times 10^5 \pm 5.2 \times 10^4$	$4.8 \times 10^{-4}$
	Seawater	$20.3 \pm 9.7$	$1.8 \times 10^{-5} \pm 1.5 \times 10^{-6}$	$0.91 \pm 0.01$	$1.3 \times 10^4 \pm 9.2 \times 10^3$	$2.1 \times 10^{-3}$

The equivalent electronic circuit used is a Randles circuit with a CPE instead of a capacitor.

**Table 4 | Alloy composition and size distribution for alloys measured using laser diffraction**

Alloy	Alloy composition (based on ICP-OES)	D10 ( $\mu\text{m}$ )	D50 ( $\mu\text{m}$ )	D90 ( $\mu\text{m}$ )
Alloy C	Al 5.0 Mn 0.8 Cr 0.6 Zr 0.17 Fe 0.24 Si	18	29	47
AlSi10Mg	Al 9.8 Si 0.33 Mg 0.15 Fe	27	48	79

Chemical compositions are in wt%, measured using ICP-OES technique. Fe, Si are considered impurities from the atomization process.



**Table 5 | Printing parameters for manufacturing samples and post processing heat treatments applied on samples**

Alloy	Heat treatment	Build plate pre-heating	Contour parameters
Alloy C AP	As-printed (no heat treatment)	150 °C	No contours
Alloy C HT	350 °C 24 hours	150 °C	No contours
AlSi10Mg	250 °C 2 hours (stress relief)	35 °C	320 W, 560 mm/s

used to train specific features from user input. It used a combination of machine learning algorithms with a set selected features described by the user to return pixel-based segmentations. The high contrast phase segmented image was then run through another plugin “SEM Particle Segmentation (beta)” developed by Rühle et al.<sup>31</sup> for getting quantitative phase data like size of the feature.

### Electrochemical measurements

To investigate the corrosion properties of the alloys, small coupons were cut from a larger printed parts and mounted in epoxy so that a 1.3 cm<sup>2</sup> area parallel to the build direction (XY) was exposed. A Cu wire was attached to the backside of the coupons to ensure electric contact. Samples were then ground with SiC paper down to P4000 grade.

Samples were then immersed in a model electrolyte of 3.5% NaCl (without pH adjustments) and in natural seawater. The seawater was taken at Kristineberg Center for Marine Research and Innovation. The average pH of the seawater was 7.86, and salinity of 31.91 psu.

After 24 hours of exposure electrochemical measurements were carried out. A PARSTAT 3000A-DX and a Gamry ECM8 Multiplexer potentiostat were used for the measurements. A three-electrode set-up was used where the working electrode was the alloy, an Ag/AgCl saturated with KCl ( $E = 0.197$  V vs SHE) was used as reference electrode, and a Pt wire or a graphite rod as the counter electrode. The open circuit potential (OCP) was first measured for 1 hour. Potentiodynamic polarisation (PD) was carried out from  $-0.25$  V vs OCP to 0 V vs Ag/AgCl with a scan rate of 1 mV/s. The Tafel module in the software VersaStudio was used to calculate the Tafel slopes and determine the corrosion current density  $I_{corr}$ . The extrapolation was carried out 0.1 V away from  $E_{corr}$ . All measurements were repeated for duplicate samples. Electrochemical Impedance Spectroscopy (EIS) was recorded in the same set-up as the potentiodynamic polarisation. An AC signal with an amplitude of  $\pm 10$  mV vs OCP was applied within a frequency range from 100 kHz to 10 mHz. The data was analysed and fitted to equivalent electronic circuits using the software ZSimpWin 3.60. Due to the noise in the measurements for the low frequencies, the data fitting was carried out only in the range of 100 kHz–100 mHz. The circuits consist of different components: resistors and constant phase elements (CPE). The CPE is used to model a non-ideal capacitor and considers the heterogeneity at the thin film surface. Its impedance can be written as  $Z_{CPE} = 1/[Y_0(j\omega)^n]$ , where  $Z_{CPE}$  is the impedance for the CPE,  $Y_0$  the modulus,  $j$  the complex number,  $\omega$  the angular frequency and  $n$  the correction factor ( $n = 1$  when the capacitor is ideal and  $0.5 < n < 1$  when it is non-ideal).  $R_s$  and  $R_{ct}$  are resistors which models the resistance of the solution and the charge transfer resistance, respectively.

### Data availability

Available from the corresponding author upon reasonable request.

Received: 23 November 2023; Accepted: 29 March 2024;

Published online: 04 May 2024

### References

1. Thijs, L., Kempen, K., Kruth, J. P. & Van Humbeeck, J. Fine-structured aluminium products with controllable texture by selective laser

melting of pre-alloyed AlSi10Mg powder. *Acta Mater.* **61**, 1809–1819 (2013).

2. Kempen, K., Thijs, L., Van Humbeeck, J. & Kruth, J. P. Mechanical properties of AlSi10Mg produced by selective laser melting. *Phys. Procedia* **39**, 439–446 (2012).
3. Revilla, R. I., Liang, J., Godet, S. & De Graeve, I. Local corrosion behavior of additive manufactured AlSiMg alloy assessed by SEM and SKPFM. *J. Electrochem. Soc.* **164**, C27–C35 (2017).
4. Leon, A., Shirizly, A. & Aghion, E. Corrosion behavior of AlSi10Mg alloy produced by additive manufacturing (AM) vs. its counterpart gravity cast alloy. *Metals* **6**, 148 (2016).
5. Shakil, S. I. et al. Additive manufactured versus cast AlSi10Mg alloy: Microstructure and micromechanics. *Results Mater.* **10**, 100178 (2021).
6. Esquivel, J., Murdoch, H. A., Darling, K. A. & Gupta, R. K. Excellent corrosion resistance and hardness in Al alloys by extended solid solubility and nanocrystalline structure. *Mater. Res. Lett.* **6**, 79–83 (2018).
7. Esquivel, J. & Gupta, R. K. Review—corrosion-resistant metastable Al alloys: an overview of corrosion mechanisms. *J. Electrochem. Soc.* **167**, 81504 (2020).
8. Trudonoshyn, O. Design of Al-Mg-Si-Mn alloys with Zn, Cr and Sc additions with unique strengthening response. (2020).
9. Mehta, B., Nyborg, L., Frisk, K. & Hryha, E. Al-Mn-Cr-Zr-based alloys tailored for powder bed fusion-laser beam process: Alloy design, printability, resulting microstructure and alloy properties. *J. Mater. Res.* **37**, 1256–1268 (2022).
10. American Society of Materials. *ASM Handbook Volume 13: Corrosion*. vol. 13 (1987).
11. Zamin, M. The role of Mn in the corrosion behavior of Al-Mn alloys. *Corrosion* **37**, 627–632 (1981).
12. Jia, Z., Hu, G., Forbord, B. & Solberg, J. K. Effect of homogenization and alloying elements on recrystallization resistance of Al-Zr-Mn alloys. *Mater. Sci. Eng. A* **444**, 284–290 (2007).
13. Knipling, K. E., Dunand, D. C. & Seidman, D. N. Precipitation evolution in Al-Zr and Al-Zr-Ti alloys during isothermal aging at 375–425 °C. *Acta Mater.* **56**, 114–127 (2008).
14. Knipling, K. E., Dunand, D. C. & Seidman, D. N. Criteria for developing castable, creep-resistant aluminum-based alloys - A review. *Int. J. Mater. Res.* **97**, 246–265 (2006).
15. Kim, Y. S. et al. Investigation of Zirconium effect on the corrosion resistance of aluminum alloy using electrochemical methods and numerical simulation in an acidified synthetic sea salt solution. *Materials* **11**, 1982 (2018).
16. Zhang, J. C. et al. Effect of Zr addition on microstructure and properties of Al-Mn-Si-Zn-based alloy. *Trans. Nonferrous Met. Soc. China (Engl. Ed.)* **24**, 3872–3878 (2014).
17. Gharbi, O. et al. Microstructure and corrosion evolution of additively manufactured aluminium alloy AA7075 as a function of ageing. *npj Mater. Degrad.* **3**, 1–11 (2019).
18. Aboulkhair, N. T. et al. 3D printing of Aluminium alloys: Additive Manufacturing of Aluminium alloys using selective laser melting. *Prog. Mater. Sci.* **106**, 100578 (2019).
19. Mehta, B., Nyborg, L., Frisk, K. & Hryha, E. Al-Mn-Cr-Zr-based alloys tailored for powder bed fusion-laser beam process: Alloy design, printability, resulting microstructure and alloy properties. *J. Mater. Res.* **3**, 1–13 (2022).
20. Mehta, B., Frisk, K. & Nyborg, L. Effect of precipitation kinetics on microstructure and properties of novel Al-Mn-Cr-Zr based alloys developed for powder bed fusion – laser beam process. *J. Alloy. Compd.* **920**, 165870 (2022).
21. Davoodi, A., Pan, J., Leygraf, C. & Norgren, S. The role of intermetallic particles in localized corrosion of an aluminum alloy studied by SKPFM and Integrated AFM/SECM. *J. Electrochem. Soc.* **155**, C211 (2008).

22. Sainis, S. & Zanella, C. A study of the localized ceria coating deposition on Fe-Rich Intermetallics in an AlSiFe Cast Alloy. *Materials* **14**, 3058 (2021).
23. Sainis, S. & Zanella, C. A localized study on the influence of surface preparation on the reactivity of cast Al-7Si-1Fe and Al-7Si-2Cu-1Fe alloys and their effect on cerium conversion coating deposition. *Appl. Surf. Sci.* **585**, 152730 (2022).
24. Fathi, P., Rafieazad, M., Duan, X., Mohammadi, M. & Nasiri, A. M. On microstructure and corrosion behaviour of AlSi10Mg alloy with low surface roughness fabricated by direct metal laser sintering. *Corros. Sci.* **157**, 126–145 (2019).
25. Ezuber, H., El-Houd, A. & El-Shawesh, F. A study on the corrosion behavior of aluminum alloys in seawater. *Mater. Des.* **29**, 801–805 (2008).
26. Zhang, S. et al. Concerning the stability of seawater electrolysis: a corrosion mechanism study of halide on Ni-based anode. *Nat. Commun.* **14**, 1–10 (2023).
27. Truesdale, G. A., Downing, A. L. & Lowden, G. F. The solubility of oxygen in pure water and sea-water. *J. Appl. Chem.* **5**, 53–62 (1955).
28. Rafieazad, M., Mohammadi, M. & Nasiri, A. M. On microstructure and early stage corrosion performance of heat treated direct metal laser sintered AlSi10Mg. *Addit. Manuf.* **28**, 107–119 (2019).
29. Mahdavian, M. & Attar, M. M. Another approach in analysis of paint coatings with EIS measurement: Phase angle at high frequencies. *Corros. Sci.* **48**, 4152–4157 (2006).
30. EOS GmbH. *EOS Aluminium AlSi10Mg Material Data Sheet EOS Aluminium AlSi10Mg Good Strength & Dynamic Load Bearing Capacity.* (2022).
31. Rühle, B., Krumrey, J. F. & Hodoroaba, V. D. Workflow towards automated segmentation of agglomerated, non-spherical particles from electron microscopy images using artificial neural networks. *Sci. Rep.* **11**, 1–10 (2021). *2021 11:1*.

## Acknowledgements

This study was performed within the European Union's Horizon 2020 research and innovation programme under grant agreement 820774, through project MANUELA- Additive Manufacturing using Metal Pilot Line. Adj. Prof. Sven Bengtsson at Högåns AB, Sweden is acknowledged for providing powder. CL and SL acknowledge RISE and AMC for funding. The

authors thank Mr. Kjell-Åke Andersson for valuable assistance with electrochemical measurements in natural seawater; and Dr. Abdelkader Meroufel for reviewing the manuscript.

## Author contributions

Conceptualization CL, BM, SS, JL, CZ, LN; Formal analysis CL, BM, SS, JL; Investigation CL, BM, SS, JL; Resources: BM, LN; Visualization CL, BM, SS, JL; Writing – Review & Editing: CL, BM, SS, JL, CZ, LN; Funding acquisition LN.

## Competing interests

The authors declare no competing interests.

## Additional information

**Correspondence** and requests for materials should be addressed to Clara Linder.

**Reprints and permissions information** is available at <http://www.nature.com/reprints>

**Publisher's note** Springer Nature remains neutral with regard to jurisdictional claims in published maps and institutional affiliations.

**Open Access** This article is licensed under a Creative Commons Attribution 4.0 International License, which permits use, sharing, adaptation, distribution and reproduction in any medium or format, as long as you give appropriate credit to the original author(s) and the source, provide a link to the Creative Commons licence, and indicate if changes were made. The images or other third party material in this article are included in the article's Creative Commons licence, unless indicated otherwise in a credit line to the material. If material is not included in the article's Creative Commons licence and your intended use is not permitted by statutory regulation or exceeds the permitted use, you will need to obtain permission directly from the copyright holder. To view a copy of this licence, visit <http://creativecommons.org/licenses/by/4.0/>.

© The Author(s) 2024